

Computationally Efficient Forward Operator for Photoacoustic Tomography Based on Coordinate Transformations

Teemu Sahlström, Aki Pulkkinen, Jarkko Leskinen, and Tanja Tarvainen

Abstract

Photoacoustic tomography (PAT) is an imaging modality that utilizes the photoacoustic effect. In PAT, a photoacoustic image is computed from measured data by modeling ultrasound propagation in the imaged domain and solving an inverse problem utilizing a discrete forward operator. However, in realistic measurement geometries with several ultrasound transducers and relatively large imaging volume, an explicit formation and use of the forward operator can be computationally prohibitively expensive. In this work, we propose a transformation based approach for efficient modeling of photoacoustic signals and reconstruction of photoacoustic images. In the approach, the forward operator is constructed for a reference ultrasound transducer and expanded into a general measurement geometry using transformations that map the formulated forward operator in local coordinates to the global coordinates of the measurement geometry. The inverse problem is solved using a Bayesian framework. The approach is evaluated with numerical simulations and experimental data. The results show that the proposed approach produces accurate three-dimensional photoacoustic images with a significantly reduced computational cost both in memory requirements and in time. In the studied cases, depending on the computational factors such as discretization, over 30-fold reduction in memory consumption and was achieved without a reduction in image quality compared to a conventional approach.

Index Terms

Photoacoustic tomography, ultrasound, coordinate transformations, computational modeling, inverse problems

I. INTRODUCTION

PHOTOACOUSTIC tomography (PAT) is an imaging modality based on the photoacoustic effect [1], [2]. In PAT, the imaging process is started by illuminating the imaged target with a short, typically nanosecond scale, light pulse. As the light is absorbed in the target, it creates areas of localized thermal expansion and pressure increase [3]. This pressure relaxes as broadband ultrasound waves that are recorded on the boundary of the imaged target. The photoacoustic image is then reconstructed from the measured photoacoustic waves by solving an inverse problem [3], [4]. Applications of photoacoustic imaging include e.g. breast cancer imaging, imaging of vasculature, small animal imaging, gastrointestinal imaging, and small animal imaging [1], [5], [6].

Various image reconstruction methods for PAT have been utilized [4]. These methods include analytic approaches such as filtered back-projection and eigenfunction expansion [7]–[10]. Furthermore, techniques based on numerical solution of the forward problem such as time-reversal [11], [12], regularized least squares techniques [13]–[16], and a Bayesian approach [17]–[20] have been utilized. The analytic methods are derived for specific measurement geometries such as planar or cylindrical, and therefore they cannot be applied in general measurement geometries. The time-reversal, regularized least squares, and Bayesian method are, on the other hand, based on a numerical approximation of the forward problem. Compared to the analytic reconstruction methods, these methods can be utilized in general measurement geometries. In addition, they offer advantages by enabling the incorporation of the measurement system specifics such as finite size and frequency response of ultrasound transducers.

A major drawback of the reconstruction methods utilizing the numerical approximation of the forward model is the high computational cost, as ultrasound propagation within the entire imaged domain has to be simulated. Furthermore, memory requirements for storing the forward operator can grow infeasibly large, especially when working with high resolution three-dimensional (3D) photoacoustic images. The requirements for a large memory overhead and computational resources have previously been alleviated using various methods. As an example, some of the memory requirements can be circumvented by exploiting inherent symmetries of the measurement setup [21]–[23]. Additionally, the forward model can be formulated such that the entries of the system matrix can be computed in a matrix-free fashion [18], [24], [25]. Furthermore, various sparsity or compressed sensing methods have been used to lessen the computational burden [26]–[28].

In this work, we propose a computationally efficient approach to the inverse problem of PAT based on coordinate transformations in the forward operator. A similar approach has been utilized in [29]. In that study, a separable forward model

Teemu Sahlström, Aki Pulkkinen, Jarkko Leskinen, and Tanja Tarvainen are with the Department of Applied Physics, University of Eastern Finland, Kuopio, Finland.

Tanja Tarvainen is also with the Department of Computer Science, University College London, London, United Kingdom.

This work was supported by the Academy of Finland (projects 314411, 336799, 312342 Centre of Excellence in Inverse Modelling and Imaging, and 320166 Flagship Program Photonics Research and Innovation), and Jane and Aatos Erkko Foundation.

was formulated for a linear ultrasound transducer array with rectangular elements. Furthermore, a coordinate transformation was utilized to simulate photoacoustic signals in a frame of reference of the ultrasound transducer in the case of point-like and linear ultrasound transducer arrays. In this work, we generalize the approach to arbitrary geometric configuration and formulate it for the inverse problem of PAT. In the approach, the discrete forward operator is constructed utilizing coordinate transformations between global coordinates that describe the forward operator of a single transducer and local coordinates of a PAT measurement geometry with various transducer positions. Furthermore, we formulate and solve the inverse problem of PAT utilizing these coordinate transformations in the forward operator.

In this work, ultrasound propagation is computationally approximated using a numerical approach based on Green's functions. The inverse problem is formulated in the framework of Bayesian inverse problems. The proposed method enables significant savings in both computation time and memory requirements compared to an explicit formation of the full forward operator while retaining the computational and implementational simplicity of matrix based approaches. Furthermore, by defining the transducer geometry using coordinate transformations, the approach can be applied in arbitrary transducer configurations as opposed to methods utilizing symmetries of the measurement setup.

The remainder of this paper is structured as follows. The forward problem of PAT and the transformation based forward operator are described in Section II. The inverse problem and the implementation of the reconstruction algorithm are described in Section III. Simulation and experimental studies are presented in Sections IV and V, respectively. Finally, results are discussed and conclusions are given in Sections VI and VII.

II. FORWARD MODEL

In PAT, propagation of ultrasound waves in a non-attenuating, homogeneous, and infinite domain Ω can be described by an initial value problem [1]

$$\begin{cases} \nabla^2 p(r, t) - \frac{1}{c^2} \frac{\partial^2 p(r, t)}{\partial t^2} = 0 \\ p(r, t = 0) = p_0(r) \\ \frac{\partial}{\partial t} p(r, t = 0) = 0, \end{cases} \quad (1)$$

where $p(r, t)$ is the pressure at position r and time instant t , c is the speed of sound, and $p_0(r)$ denotes the instantaneous initial pressure generated by the photoacoustic effect. In practice, the photoacoustic signal that samples $p(r, t)$ is measured on a finite number of points or surfaces around the imaged domain. The assumptions for non-attenuating and homogeneous domain have been shown to produce accurate photoacoustic images in soft-tissue or soft-tissue mimicking targets [14], [15], [17]–[19]. However, if the target is composed of heterogeneous tissues such as soft-tissue and bone, the homogeneous model could still be useful when the modeling errors are taken into account [30].

In this work, the solution of the wave equation (1) is approximated by the solution of a reformulated wave-equation [31], [32]

$$\nabla^2 p(r, t) - \frac{1}{c^2} \frac{\partial^2 p(r, t)}{\partial t^2} = \frac{1}{c^2} p_0(r) \frac{\partial}{\partial t} \nu(t), \quad (2)$$

where $\nu(t) \geq 0$ is a temporal distribution describing the formation of the initial pressure $p_0(r)$ in the domain. As the temporal width of $\nu(t)$ approaches zero, (2) becomes a better approximation of (1).

The solution of the wave-equation (2) can be written as a convolution of the initial pressure p_0 and the Green's function \mathcal{G} of Eq. (2) [33]

$$p(r, t) = \int_{\Omega} p_0(\tilde{r}) \mathcal{G}(r - \tilde{r}, t) d\tilde{r}, \quad (3)$$

where r denotes the observation position and \tilde{r} is a position in domain Ω . Furthermore, \mathcal{G} in (3) can be written as

$$\mathcal{G}(r - \tilde{r}, t) = \frac{1}{c^2} \mathcal{F}^{-1} \left\{ i\omega \hat{\nu}(\omega) \hat{\mathcal{G}}(\|\tilde{r} - r\|, \omega) \right\} (t), \quad (4)$$

where \mathcal{F}^{-1} is the inverse Fourier transform, i is the imaginary unit, ω is the angular frequency, and $\hat{\nu}$ is the Fourier transform of ν . In 3D, $\hat{\mathcal{G}}$ is the Green's function of the Helmholtz equation defined as [33]

$$\hat{\mathcal{G}}(\|\tilde{r} - r\|, \omega) = \frac{1}{4\pi\|\tilde{r} - r\|} \exp\left(i\frac{\omega}{c}\|\tilde{r} - r\|\right). \quad (5)$$

In this work, the initial pressure distribution $p_0(r)$ is discretized using a tetrahedral mesh. The discretized initial pressure $p_{0,l}$ is defined using L piecewise linear basis functions χ_l , $l = 1, \dots, L$, centered at the grid nodes. The initial pressure can then be approximated as

$$p_0(r) \approx \sum_{l=1}^L p_{0,l} \chi_l(r). \quad (6)$$

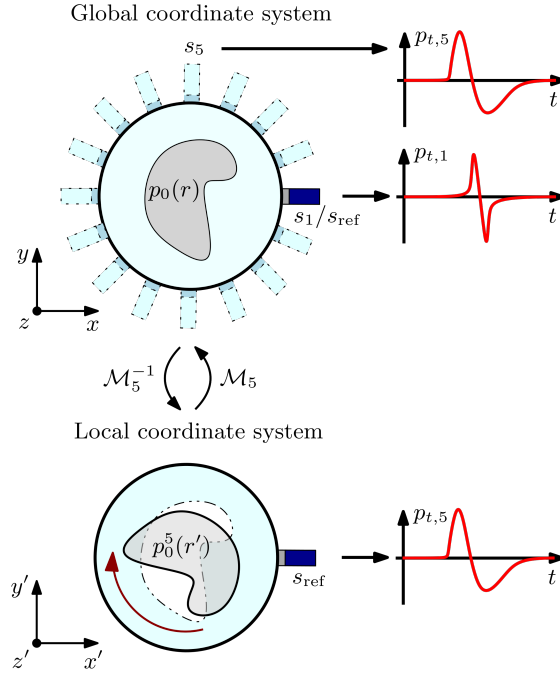


Fig. 1. Principle of the transformation based forward model in PAT. In the transformation based forward model, the photoacoustic signals are computed in a local coordinate system using a reference transducer position. These are transformed to the transducers in the global coordinate system using mappings \mathcal{M}_n . In the figure, an example of the transformation-based forward model in the case of a rotation is illustrated. In this situation, the reference transducer (shown as the dark blue rectangle) is chosen as s_1 . The recorded signal for the fifth transducer s_5 can then be simulated in the local coordinate system by rotating the initial pressure distribution $p_0(r)$ to the orientation corresponding to transducer s_5 .

Using the discretized initial pressure, the solution of the wave equation (2) can be approximated as

$$p(r, t) \approx \sum_{l=1}^L p_{0,l} \int_{\Omega} \chi_l(\tilde{r}) \mathcal{G}(r - \tilde{r}, t) d\tilde{r}, \quad (7)$$

where the integral is approximated using, for example, Gaussian quadratures. In addition to the outlined approach of using Green's functions, ultrasound propagation could also be simulated using other methods such as the k -space time-domain method [34].

Consider now a measurement setup consisting of N ultrasound transducers at positions $s_n, n = 1, \dots, N$. Further, let the recorded photoacoustic signal be discretized using M temporal points. Then, the discretized conventional forward model for PAT can be written as

$$p_{t,\text{CNV}} = K_{\text{CNV}} p_0 \quad (8)$$

where $p_{t,\text{CNV}} \in \mathbb{R}^{MN}$ is a vector containing photoacoustic time-series of each ultrasound transducer, $K_{\text{CNV}} \in \mathbb{R}^{MN \times L}$ is a discrete forward operator describing (7), and $p_0 = \{p_{0,1} \dots p_{0,L}\}^T \in \mathbb{R}^L$ is the discretized initial pressure. In practice, the discrete forward operator can be formed by simulating the impulse responses for each of the nodes of the domain Ω and placing the resulting wave-forms on the columns of the forward operator.

A. Transformation based forward model

Let us now define global (laboratory) and local (transducer) coordinate systems denoted by r and r' respectively. A coordinate mapping \mathcal{M}_n for each ultrasound transducer position between the global and local coordinate systems can then be written as

$$r = \mathcal{M}_n(r') = R_n r' + T_n \quad (9)$$

where R_n is a rotation matrix and $T_n = \{T_{x,n} T_{y,n} T_{z,n}\}^T$ is a translation vector corresponding to the n :th ultrasound transducer position.

Using the coordinate mapping \mathcal{M}_n , the initial pressure $p_0(r)$ in the global coordinate system and the initial pressures $p_0^n(r')$ corresponding to the transducer positions in the local coordinate system can be written as

$$p_0(r) = p_0^n(\mathcal{M}_n^{-1}(r)) \quad (10)$$

$$p_0^n(r') = p_0(\mathcal{M}_n(r')), \quad (11)$$

$$\Gamma_{p_0} Q^T \text{vec} \left(K_{\text{REF}}^T \left(\Gamma_e^{-1} \text{vec} \left(K_{\text{REF}} (Q \eta_{p_0|p_t})_{L \times N} \right) \right)_{N \times M} \right) + \eta_{p_0|p_t} = \Gamma_{p_0} \left(Q^T \text{vec} \left(K_{\text{REF}} \left(\Gamma_e^{-1} (p_t - \eta_e) \right)_{N \times M} \right) \right) + \eta_{p_0} \quad (24)$$

as visualized in Fig. 1.

Let us now choose a reference transducer location such that in the local coordinate system

$$p_{t,\text{REF}} = K_{\text{REF}} p_0, \quad (12)$$

where $p_{t,\text{REF}} \in \mathbb{R}^M$ is the photoacoustic time-series for a reference point and $K_{\text{REF}} \in \mathbb{R}^{M \times L}$ is the corresponding discrete forward operator. Furthermore, let $Q_n \in \mathbb{R}^{L \times L}$ be an interpolation matrix approximating the mapping (11) in a discrete setting i.e.

$$p_0^n = Q_n p_0. \quad (13)$$

In this work, the interpolation matrix Q_n describes linear interpolation utilizing barycentric coordinates over the tetrahedral elements.

Utilizing the mapping (13), a transformation based forward model for the n :th transducer in the local coordinates can now be written as

$$p_{t,\text{TRN}}^n = K_{\text{REF}} Q_n p_0. \quad (14)$$

The problem of solving the photoacoustic time-series for each transducer in the global coordinate system is thus equivalent to solving the photoacoustic time-series for a reference transducer in the local coordinates for multiple orientations of the initial pressure.

Using (14), the numerical implementation of the forward model (8) can be approximated as

$$\begin{aligned} p_{t,\text{TRN}} &\approx \begin{bmatrix} K_{\text{REF}} Q_1 \\ K_{\text{REF}} Q_2 \\ \dots \\ K_{\text{REF}} Q_N \end{bmatrix} p_0 \\ &= K_{\text{TRN}} p_0, \end{aligned} \quad (15)$$

This approximation reduces the memory requirements with respect to storing the forward operator $K_{\text{CNV}} \in \mathbb{R}^{MN \times L}$ into storing the forward operator $K_{\text{REF}} \in \mathbb{R}^{M \times L}$ and N sparse matrices $Q_n \in \mathbb{R}^{L \times L}$. In the case of tetrahedral mesh, every row of Q_n contains at most four nonzero elements. As an example, using a mesh with 10^6 nodes, a fraction of $4 \cdot 10^{-8}$ of the entries of Q_n are nonzero.

III. INVERSE PROBLEM

In this work, the inverse problem of PAT is approached in a Bayesian framework [17], [19], [35]. In the approach, all parameters are modeled as random variables, and it combines the information obtained through the measurements, forward model, and prior model for the unknown parameters. The solution of the inverse problem, i.e. the posterior distribution, is given by the Bayes' formula [35]

$$\pi(p_0|p_t) \propto \pi(p_t|p_0)\pi(p_0), \quad (16)$$

where $\pi(p_t|p_0)$ is the likelihood distribution and $\pi(p_0)$ is the prior distribution.

The discrete observation model for PAT can be written as

$$p_t = K p_0 + e, \quad (17)$$

where $p_t \in \mathbb{R}^{MN}$ is a vector of measured photoacoustic waves, K and p_0 are the discretized forward operator and initial pressure, and $e \in \mathbb{R}^{MN}$ is additive measurement noise [35]. Assume now, that the initial pressure p_0 and the measurement error e are mutually independent, and that the measurement error is Gaussian distributed $e \sim \mathcal{N}(\eta_e, \Gamma_e)$, where $\eta_e \in \mathbb{R}^{MN}$ is the expected value and $\Gamma_e \in \mathbb{R}^{MN \times MN}$ is the covariance matrix. The likelihood distribution can then be written as [35]

$$\pi(p_t|p_0) \propto \exp \left\{ -\frac{1}{2} \|L_e(p_t - K p_0 - \eta_e)\|_2^2 \right\}, \quad (18)$$

where L_e is the Cholesky decomposition of the inverse covariance matrix of the measurement error $\Gamma_e^{-1} = L_e^T L_e$.

Let us further model the initial pressure as Gaussian distributed $p_0 \sim \mathcal{N}(\eta_{p_0}, \Gamma_{p_0})$, where $\eta_{p_0} \in \mathbb{R}^L$ is the expected value and $\Gamma_{p_0} \in \mathbb{R}^{L \times L}$ is the covariance matrix. Then, the posterior distribution can be written as

$$\pi(p_0|p_t) \propto \exp \left\{ -\frac{1}{2} (\|L_e(p_t - Kp_0 - \eta_e)\|_2^2 + \|L_{p_0}(p_0 - \eta_{p_0})\|_2^2) \right\}. \quad (19)$$

Now, in the case of a linear observation model and Gaussian distributed noise and parameters, the posterior distribution (19) is also Gaussian $p_0|p_t \sim \mathcal{N}(\eta_{p_0|p_t}, \Gamma_{p_0|p_t})$, where $\eta_{p_0|p_t}$ is the expected value and $\Gamma_{p_0|p_t}$ is the covariance matrix. The expected value of the posterior distribution, which corresponds to the *maximum a posteriori* (MAP) estimate, can be computed by solving a linear system of equations of the form

$$H\eta_{p_0|p_t} = d, \quad (20)$$

where

$$H = \Gamma_{p_0} K^T \Gamma_e^{-1} K + I, \quad (21)$$

$$d = \Gamma_{p_0} K^T \Gamma_e^{-1} (p_t - \eta_e) + \eta_{p_0}, \quad (22)$$

and I is an identity matrix [17], [35]. Furthermore, the covariance matrix $\Gamma_{p_0|p_t}$ is given by

$$\Gamma_{p_0|p_t} = (K^T \Gamma_e^{-1} K + \Gamma_{p_0}^{-1})^{-1}. \quad (23)$$

In this work, the MAP-estimates $\eta_{p_0|p_t}$ are solved iteratively using both conventional forward operator K_{CNV} , Eq. (8), and the transformation based forward operator K_{TRN} , Eq. (15), using the general minimum residual method (GMRES) inbuilt in MATLAB. Solving (20) as is using $K = K_{\text{CNV}}$ can, however, be computationally prohibitively expensive in realistic 3D measurement geometries with several ultrasound transducers and dense spatial discretization.

The computational cost associated with the conventional forward model can be alleviated by utilizing the transformation based approach. Let us first define a total interpolation matrix $Q \in \mathbb{R}^{N \times L}$ as a matrix, where the interpolation matrices Q_n are stacked column-wise. Then, using the derivation of the MAP-estimate and the transformation based forward model (15), the linear system of equations (20) can be written as shown in (24), where $\text{vec}(\cdot)$ denotes a column-wise vectorization of a matrix and $(\cdot)_{A \times B}$ denotes a column-wise matrix reshaping operation resulting in a matrix with A rows and B columns. This enables the efficient computation of the MAP-estimate.

A. Prior distribution

In the Bayesian framework for inverse problems, prior information about the imaged target is included in the solution of the inverse problem via the prior distribution. In this work, a Gaussian piece-wise polynomial prior distribution is used. It is defined by its mean η_{p_0} and a covariance function [36]

$$\Gamma_{p_0} = \begin{cases} \tilde{\sigma}_{p_0}^2 (\kappa - \|r_i - r_j\|)^b, & \text{for } \kappa - \|r_i - r_j\| > 0 \\ 0, & \text{for } \kappa - \|r_i - r_j\| \leq 0, \end{cases} \quad (25)$$

where κ is a constant controlling the spatial correlation, $r_{i,j}$ are positions of the discretization points and $\tilde{\sigma}_{p_0}^2 = \sigma_{p_0}^2 / \kappa^b$, σ_{p_0} is the standard deviation. Furthermore, the power b is defined as $b = (D/2) + q + 1$, where D is the spatial dimension of the problem and q is a constant.

The parameters κ and q control the shape of the covariance function. Thus by the choice of these parameters, the covariance function (25) can be tuned to closely match the Ornstein-Uhlenbeck process that has previously been utilized in PAT [17]–[19], [32]. The advantage of the piece-wise polynomial covariance function, compared to the Ornstein-Uhlenbeck process, is that the values of the covariance become exactly zero after some distance κ . Therefore, when using small values of κ , the covariance matrix can be stored as a sparse matrix conserving computer memory.

IV. SIMULATIONS

In the numerical simulation studies, forward solutions using the transformation based forward model were compared against the conventional forward model using various levels of spatial discretizations and lengths of the light pulses. Furthermore, the solution of the inverse problem was studied using various spatial discretizations, light pulse durations, and measurement noise levels.

Computations were performed with MATLAB (R2016b, The MathWorks, Inc., Natick, MA) using a PC with two Intel Xeon E5-2630 CPUs @2.20 GHz and 256 GB of random access memory.

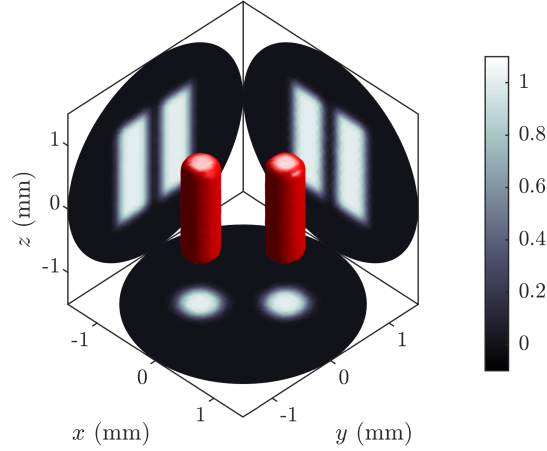


Fig. 2. Initial pressure of the numerical phantom used in the comparison of the forward solutions and reconstructions. Thresholded value on the surface of the phantom is shown as red (threshold value 0.5). Maximum intensity projections in the x -, y -, and z -directions are shown as 2D grayscale images.

TABLE I

SPATIAL AND TEMPORAL DISCRETIZATIONS USED IN THE COMPARISON OF THE FORWARD MODELS. AVERAGE LENGTH Δh AND STANDARD DEVIATION OF THE ELEMENT SIDE LENGTHS, NUMBER OF NODES AND ELEMENTS IN THE SPATIAL DISCRETIZATION, LENGTH OF TIME STEP Δt , AND NUMBER OF TIME POINTS M IN THE TEMPORAL DISCRETIZATION

Δh (μm)	Nodes	Elements	Δt (ns)	M
142 ± 28	9030	46104	41.9	202
115 ± 23	15836	85115	33.9	249
88 ± 15	36273	195472	29.4	286

TABLE II

STANDARD DEVIATIONS (SD) AND FULL WIDTH HALF MAXIMUM VALUES (FWHM) FOR THE LIGHT PULSES ν_{1-8} USED IN THE COMPARISON OF THE FORWARD MODELS

	ν_1	ν_2	ν_3	ν_4	ν_5	ν_6	ν_7	ν_8
SD (ns)	200	150	100	80	60	40	20	10
FWHM (ns)	471	353	234	188	141	94	47	24

A. Comparison of forward solutions

The validity of the transformation based forward model (15) was compared against the conventional forward model (8) by comparing and simulating photoacoustic data using different discretizations. In the simulations, a domain consisting of a 1.5 mm radius ball was considered. The measurement geometry consisted of 300 point-like ideal ultrasound transducers which were distributed equidistantly on a sphere with a radius of 5.05 mm. The initial pressure used in the simulations is shown in Fig. 2. The speed of sound was set to $c = 1500$ m/s.

The forward solutions were computed using three spatial and temporal discretizations. In this work, all temporal discretizations were chosen such that $\Delta t = \Delta x_{\min}/c$, where Δt is the time step and Δx_{\min} is the shortest tetrahedron side length in the spatial discretization. Furthermore, the number of time steps M was chosen based on the time of flight (TOF) of the ultrasound waves in the domain such that $M \geq \text{TOF}/\Delta t$. The average length of the vertices, the number of nodes and elements, and the length and number of time steps are shown in Table I. The light pulse ν in the wave equation (2) was modeled as Gaussian. Eight light source pulse lengths $\nu_i, i = 1, \dots, 8$ shown in Table II were considered. The studied initial pressure was linearly interpolated to each of the discretizations.

Photoacoustic data $p_{t,\text{TRN}}$ was simulated by the proposed approach using coordinate transformations (15). This was compared against photoacoustic data $p_{t,\text{CNV}}$ simulated using a conventional approach (8) where the full forward operator K_{CNV} was employed. The solutions were compared by computing relative errors

$$E_{\text{FWD}} = 100\% \cdot \frac{\|p_{t,\text{CNV}} - p_{t,\text{TRN}}\|}{\|p_{t,\text{CNV}}\|}. \quad (26)$$

These are shown in Table III.

From the relative errors, it can be seen that the modeling errors of the transformation-based forward model increase with decreasing length of the light pulse and coarser discretization. These errors can be explained by the varying levels of interpolation

TABLE III
RELATIVE ERRORS $E_{\text{FWD}}(\%)$ OF THE FORWARD SOLUTIONS FOR LIGHT PULSES ν_{1-8} AND THREE DISCRETIZATIONS WITH AN AVERAGE LENGTH OF THE VERTICES Δh

Δh (μm)	$E_{\text{FWD}}(\%)$							
	ν_1	ν_2	ν_3	ν_4	ν_5	ν_6	ν_7	ν_8
142	1.3	2.1	3.3	3.9	4.7	5.7	14.2	22.2
115	0.9	1.4	2.1	2.5	3.1	3.8	7.1	17.0
88	0.5	0.8	1.3	1.5	1.8	2.3	3.6	9.0

TABLE IV
SPATIAL AND TEMPORAL DISCRETIZATIONS USED IN DATA SIMULATION. AVERAGE LENGTH Δh AND STANDARD DEVIATION OF THE ELEMENT SIDE LENGTHS, NUMBER OF NODES AND ELEMENTS IN THE SPATIAL DISCRETIZATION, LENGTH OF TIME STEP Δt , AND NUMBER OF TIME POINTS M IN THE TEMPORAL DISCRETIZATION

Δh (μm)	Nodes	Elements	Δt (ns)	M
43 ± 7	287085	1622008	13.7	613

errors within the transformation based forward model. As the spatial discretization becomes denser, the interpolation errors get smaller. Furthermore, as the light pulse becomes shorter, interpolation error increase.

B. Comparison of reconstructions

The validity of the transformation-based forward operator in the inverse problem of PAT was studied by solving the inverse problem with various discretizations, lengths of the light pulse, and measurement noise levels. The reconstructions were compared against reconstructions computed using the conventional forward operator. In the simulations, the same target volume (1.5 mm radius ball), transducer geometry, and initial pressure (Fig. 2) as in the comparison of the forward models were used.

1) *Data Simulation:* Photoacoustic data was simulated using the solution of the wave-equation (7). Spatial and temporal discretizations used in data simulation are shown in Table IV. The temporal light pulse in (7) was modeled as Gaussian with varying lengths (Table II).

To study the effect of measurement noise, five levels $\epsilon_i, i = 1, \dots, 5$ of uncorrelated Gaussian distributed zero-mean noise was added to the data. The noise levels were chosen such that standard deviation σ_e was set to 0.1, 0.5, 1.0, 2.0, and 4.0% of the maximum simulated pressure value in the data for the light pulse length ν_1 . These noise levels corresponded to signal to noise ratios of 42.9, 29.0, 23.1, 17.0, and 10.0 dB, which were used to determine the noise levels for the light pulses ν_{2-8} .

2) *Inverse Problem:* In the inverse problem, the spatial and temporal discretizations were the same as in the comparison of the forward model (Table I). Furthermore, in the simulations for the model matrices K_{CNV} and K_{REF} , the light pulses were modeled as Gaussian using the same parameters as in the comparison of the forward models (Table II).

The prior distribution used in the inverse problem was a Gaussian distribution with the expected value of $\eta_{p_0} = 0.5$ that is equal to the mean between the minimum and maximum values of the simulated initial pressure. Further, the covariance was the piece-wise polynomial distribution (25) with the parameters $\sigma_{p_0} = 1/2$, $\kappa = 1200 \mu\text{m}$, $D = 3$, and $q = 3$. The standard deviation was chosen such that the values of the initial pressure lied within ± 1 standard deviation from the expected value. Using these values, the piece-wise polynomial covariance function approximates an Ornstein-Uhlenbeck process with a characteristic length of $\ell = 0.4 \text{ mm}$. Measurement noise statistics were modeled using the same parameters as in the data simulation.

MAP-estimates were computed utilizing the transformation based forward model by solving the system of equations (24) using the GMRES method. The iterations were computed until the relative residual of the iteration was less than 10^{-6} that was found to ensure the convergence of the iteration. The initial guess of the iteration was set similar to Ref. [18] as

$$\eta_{p_0|p_t, \text{init}} = \alpha \tilde{p}_0, \quad (27)$$

where

$$\tilde{p}_0 = Q^T \text{vec} (K_{\text{REF}}^T (p_t)_{M \times N}), \quad (28)$$

and α is a solution of a minimization problem

$$\alpha = \arg \min_{\alpha} \|p_t - \alpha K_{\text{REF}} (Q \tilde{p}_0)_{L \times N}\| \quad (29)$$

$$= \frac{p_t (K_{\text{REF}} (Q \tilde{p}_0)_{L \times N})}{(K_{\text{REF}} (Q \tilde{p}_0)_{L \times N})^T K_{\text{REF}} (Q \tilde{p}_0)_{L \times N}}. \quad (30)$$

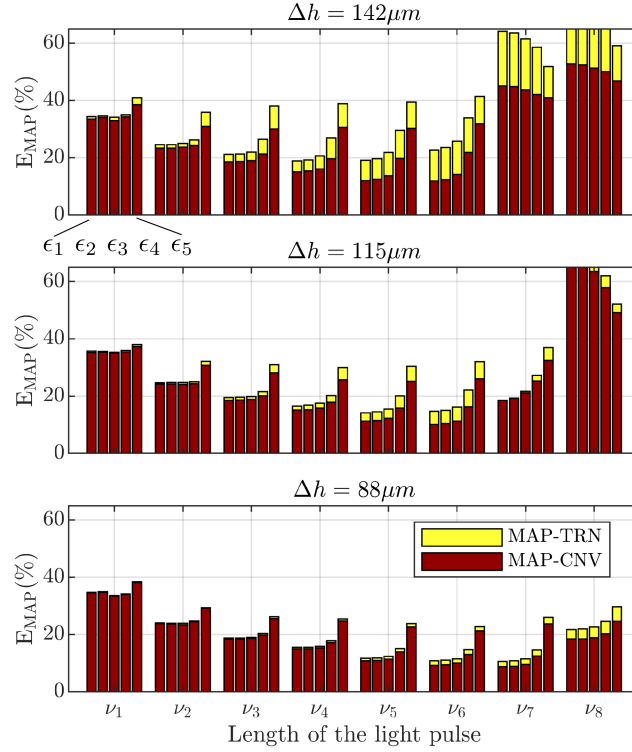


Fig. 4. Relative errors of the MAP-CNV and MAP-TRN estimates at discretizations $\Delta h = 142, 115,$ and $88 \mu\text{m}$. For each light pulse ν_{1-8} , relative errors at five measurement noise levels ϵ_{1-5} are presented.

TABLE V
MEMORY REQUIREMENT AND TIME TO ASSEMBLE THE MATRIX SEPARATED BY THE SLASH-SYMBOL FOR THE CONVENTIONAL FORWARD OPERATOR K_{CNV} , AND THE PROPOSED TRANSFORMATION BASED FORWARD OPERATOR BASED ON K_{REF} AND INTERPOLATION MATRIX Q AT EACH DISCRETIZATION LEVEL Δh

Δh (μm)	K_{CNV} (GB)/(s)	K_{REF} (GB)/(s)	Q (GB)/(s)
142	4.38 / 323.1	0.01 / 2.9	0.14 / 4.1
115	9.46 / 738.9	0.03 / 7.9	0.26 / 6.0
88	24.9 / 1522.1	0.08 / 17.5	0.62 / 13.3

by defining the light pulse in a different manner. Furthermore, the total reconstruction time, total time used in the GMRES-iterations and number of GMRES-iterations using the conventional model and the transformation based model for light pulse ν_6 and noise level ϵ_3 are shown in Table VI for each discretization level Δh . As it can be seen, the forward operator K_{REF} can be computed significantly faster and requires much less memory compared to K_{CNV} . Additionally, the reconstruction times using the transformation based model are lower compared to the conventional model.

C. Blood vessel mimicking numerical phantom

Then, in order to simulate a more realistic target, a blood vessel mimicking numerical phantom was considered. The target domain consisted of a ball with a radius of 5 mm. The initial pressure was constructed of blood vessel mimicking structures illustrated in Fig. 5. The measurement setup consisted of 1000 point-like ideal ultrasound transducers distributed evenly on a sphere with a radius of 5.05 mm.

1) *Data simulation:* Photoacoustic data was simulated with the wave equation using (7). The spatial and temporal discretizations used in the data simulation are shown in Table VII. The light pulse ν in (2) was modeled as Gaussian with standard deviation of 20 ns (light pulse ν_7 of simulations of Table II). Further, uncorrelated zero-mean Gaussian noise was added to the data. Standard deviation of the noise was chosen such that the SNR was equal to approximately 23.5 dB (approximately noise level ϵ_3 of the previous simulations). This corresponded to a standard deviation σ_e of approximately 0.5% of the maximum simulated value.

2) *Inverse problem:* The spatial and temporal discretizations used in the inverse problem are given in Table VII. The prior distribution used in computing the MAP-estimate was the Gaussian piece-wise polynomial prior distribution (25). The expected value and standard deviation of the prior distribution were set to $\eta_{p_0} = 0.5$ and $\sigma_{p_0} = 0.5$ respectively. Furthermore,

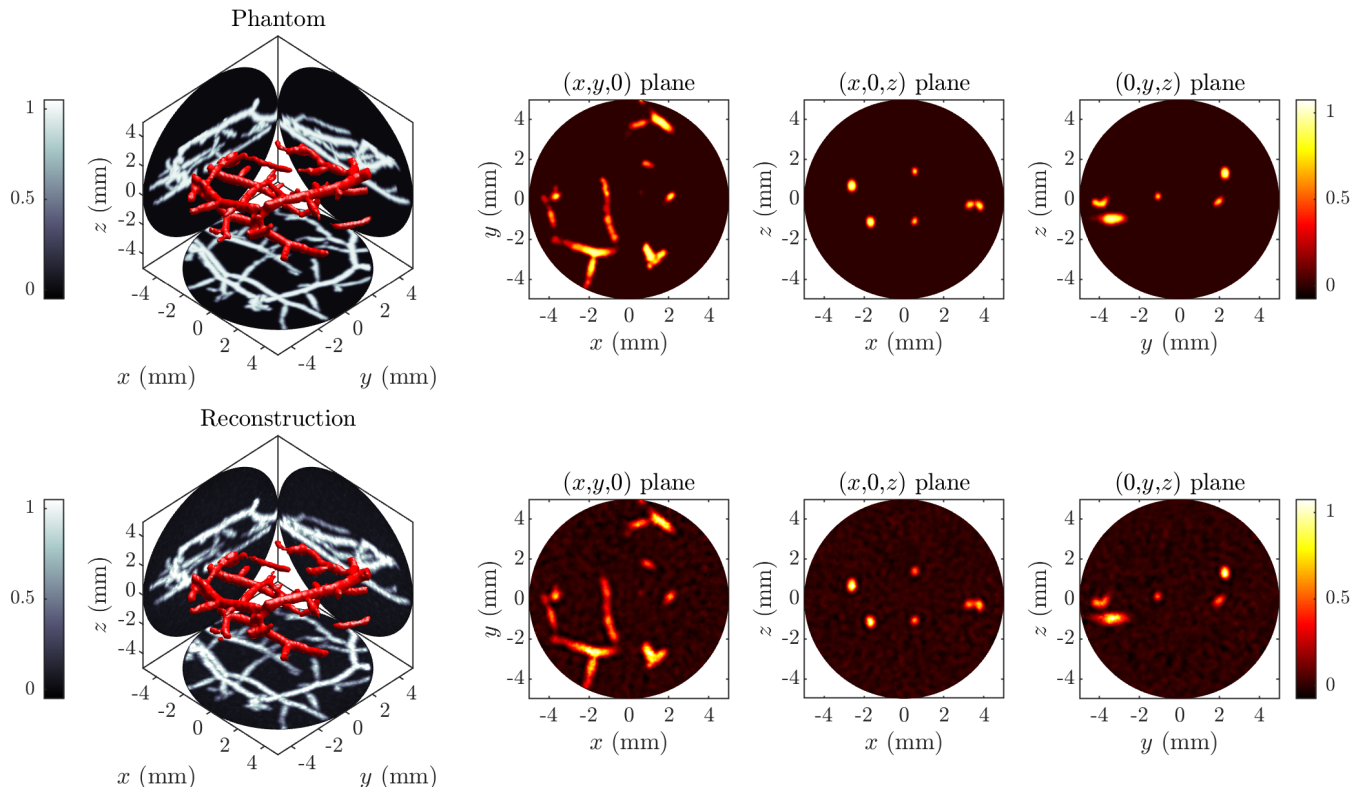


Fig. 5. Simulated (top row) and estimated (bottom row) initial pressure in the numerical vessel phantom. Images from left to right: a thresholded volumetric plot of the initial pressure (threshold value of 0.3) with maximum intensity projections in the x -, y -, and z -directions (first column) and cross sections of the initial pressure on $(x,y,0)$, $(x,0,z)$ and $(0,y,z)$ planes (columns 2-4).

TABLE VI
TOTAL RECONSTRUCTION TIMES t_{REC} , TOTAL TIME USED IN THE GMRES ITERATIONS t_{ITER} AND NUMBER OF ITERATIONS FOR THE RECONSTRUCTIONS USING THE CONVENTIONAL AND TRANSFORMATION BASED MODEL FOR EACH DISCRETIZATION Δh . THE DATA SHOWN IS BASED ON RECONSTRUCTIONS WITH LIGHT PULSE ν_6 AND NOISE LEVEL ϵ_3

Δh (μm)	Conventional model			Transformation based		
	t_{REC} (s)	t_{ITER} (s)	Iter. count	t_{REC} (s)	t_{ITER} (s)	Iter. count
142	32.2	0.20	160	20.9	0.12	181
115	62.6	0.43	144	37.7	0.24	157
88	156.1	1.13	138	114.9	0.80	144

the parameters controlling the structure of the covariance function were chosen as $\kappa = 1080 \mu\text{m}$, $D = 3$, and $q = 3$. These parameter choices approximate the Ornstein-Uhlenbeck process with a characteristic length of $\ell = 0.18 \text{ mm}$. The measurement noise was modeled as uncorrelated zero-mean Gaussian with a standard deviation equal to the noise added to the simulated measurement data.

MAP-estimate utilizing the transformation-based forward model was computed by solving the system of equations (24) using the GMRES method. The iterations were computed until a relative residual of $3 \cdot 10^{-5}$, which was confirmed to guarantee convergence of the iteration. With this criterion, the iteration converged in 85 iterations with the computation time of 10 hours and 35 minutes (approximately 370 seconds per iteration). The initial guess was set similarly as earlier using (27). The memory requirements for the interpolation matrix Q and the forward operator K_{REF} were 74.8 GB and 3.2 GB respectively. The results could not be compared against the conventional approach in which the whole forward operator had been formulated. This was due to the 3171.6 GB memory requirement of the full forward operator K_{CNV} . Instead, a time-reversal reconstruction was computed to provide a comparison result. This is presented in the supplementary material.

3) *Results:* The numerical blood-vessel like phantom and the MAP-estimate are shown in Fig. 5. As it can be seen, the reconstruction using the transformation-based forward model is able to distinguish the vessel-like details of the phantom. Furthermore, even the smaller structures of the phantom are facilitated by the relatively dense spatial discretization.

TABLE VII
 SPATIAL AND TEMPORAL DISCRETIZATIONS USED IN THE DATA SIMULATION AND INVERSE PROBLEM FOR THE BLOOD VESSEL MIMICKING PHANTOM. AVERAGE LENGTH Δh AND STANDARD DEVIATION OF THE ELEMENT SIDE LENGTHS, NUMBER OF NODES AND ELEMENTS IN THE SPATIAL DISCRETIZATION, LENGTH OF TIME STEP Δt , AND NUMBER OF TIME POINTS M IN THE TEMPORAL DISCRETIZATION

	Δh (μm)	Nodes	Elements	Δt (ns)	M
Data simulation	87 ± 15	1231086	7054660	20.5	362
Inverse problem	89 ± 16	1197719	6915553	22.4	331

V. EXPERIMENTAL STUDY

A. Measurement setup

The measurement setup consisted of a Nd:YAG laser and an optical parametric oscillator (model NT352B-10, Ekspla Uab, Lithuania), which provided 3 ns long pulses at 700 nm wavelength at a repetition rate of 10 Hz. The pulses were guided through an optical fiber and collimated using a plano-convex lens into approximately 14 mm diameter beam. The pulse energy was set to 1 mJ. Photoacoustic waves were measured using a circular cylindrically focused PZT transducer (model V383, Olympus NDT, MA, USA; aperture diameter 9.53 mm, focal distance 33 mm) connected to a receiver (model 5800 PR, Olympus NDT; pass-band 0.1 to 10 MHz, gain 40 dB). The transducer had a central frequency of 3.4 MHz and a FWHM bandwidth from 1.7 MHz to 5.1 MHz. The focal FWHM dimensions were 6.2 mm, 13 mm, and 1.6 mm in lateral, axial, and elevational directions, respectively.

The imaged target was made of 210 μm diameter black fishing line (Berkley FireLine Fused MicroIce, Pure Fishing Inc., SC, USA). The line was tied to a structure consisting of two loops separated by a knot with loose ends. To form a 3D structure, one of the loops was lifted approximately 80 degrees from the horizontal xy plane to the vertical yz plane. Dimensions of the loops were 3 mm and 2 – 2.5 mm in the yz and xy planes, respectively. The knot was cast inside a phantom made of water, gelatin (10%, Sigma-Aldrich, MO, USA), intralipid (1%, Fresenius Kabi AB, Uppsala, Sweden), and Indian ink (Royal Talens, the Netherlands). Guidelines for homogeneous gelatin-Intralipid phantom manufacturing were followed [37]. Optical absorption [38] and reduced scattering [39] were 0.1 cm^{-1} and 10 cm^{-1} , respectively. The cylindrical phantom had a height of 13.4 mm and a diameter of 13 mm. The line structure was positioned at the center of the phantom. The phantom was immersed in a water tank filled with room temperature deionized and degassed water. Visualization of the target and the phantom are presented in Fig. 6 a) and b).

Laser pulses were administered above the phantom (z-direction) through the air-water interface. The transducer was moved around the phantom in seven elevational (z-directional) planes using 0.5 mm increments. Furthermore, for every plane, the transducer was rotated 185 degrees with increments of 1 degree on a 32.4 mm radius circle. In total, this resulted in 1295 transducer positions. The photoacoustic data was sampled at 100 MHz and averaged over 10 consecutive measurements using an oscilloscope (model 6051A WR, LeCroy Inc., NY, USA). Visualization of the measurement geometry is shown in Fig. 6 c).

B. Inverse problem

For the inverse problem, a cylindrical computation domain with a height of 6 mm and a radius of 4.5 mm was considered. The spatial and temporal discretizations are given in Table VIII. The light pulse ν was modeled as Gaussian with a length (standard deviation) of 10 ns, which was the approximate shortest length of the light pulse supported by the temporal discretization. The speed of sound was determined according to the temperature of the water and set to $c = 1483 \text{ m/s}$.

The response of the finite-sized transducer was modeled using a patch-based approach [40] by discretizing the surface of the transducer in 6488 points on an equidistant grid and averaging the recorded wave-forms. The discretization Δh_s , i.e. the distance between adjacent points on the transducer surface was chosen such that $\Delta h_s = \lambda_{\text{max}}/2$, where λ_{max} is the wavelength of the maximum supported frequency of the ultrasound transducer ($\sim 7 \text{ MHz}$). The frequency response of the ultrasound transducer was modeled according to the specifications of the transducer by including a frequency domain filtering operation to the forward operator.

Prior distribution used in the reconstructions was the Gaussian polynomial based prior distribution (25). Expected value was set to $\eta_{p_0} = 0$. Standard deviation was set to $\sigma_{p_0} = 0.25$. Parameters for the piece-wise polynomial covariance matrix were set to $\kappa = 300 \mu\text{m}$, $D = 3$, and $q = 3$. Statistics of the measurement noise were evaluated from a 500 time point measurement signal preceding the illumination. The standard deviation of the measurement noise for each transducer was between $3.9 \cdot 10^{-3}$ and $7.2 \cdot 10^{-3}$ and the expected value between $-2.3 \cdot 10^{-3}$ and $2.5 \cdot 10^{-3}$. For reference, the maximum value of the recorded signal was 0.13.

The MAP-estimate was computed by solving the system of equations (24) using the GMRES method. The initial guess for the iteration was set as in the simulations using (27). The iteration was ended when the relative residual reached the value of 10^{-6} . This resulted in 11 iterations and a reconstruction time of approximately 1250 seconds. The memory requirement for the interpolation matrix Q and the single transducer forward operator K_{REF} were 49.0 GB and 2.3 GB, respectively. Due to

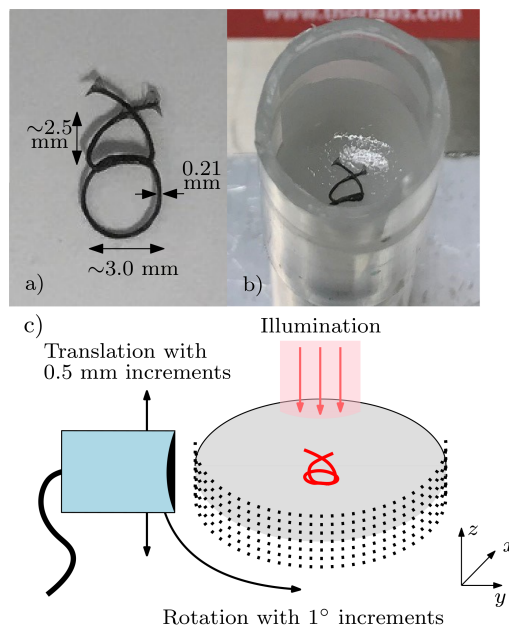


Fig. 6. Visualization of the experimental setup and phantom used in the study. (a) Flat un-cast fishing line knot with two loops. (b) Partially cast knot with the bottom loop twisted towards the vertical yz plane. (c) Visualization of the measurement geometry. In the setup, the ultrasound transducer (shown in blue) is rotated 185° around the imaged target (shown as the red knot) with 1° increments on seven planes with 0.5 mm increments (black dots).

TABLE VIII

SPATIAL DISCRETIZATIONS USED IN THE INVERSE PROBLEM FOR THE EXPERIMENTAL PHANTOM. AVERAGE LENGTH Δh AND STANDARD DEVIATION OF THE ELEMENT SIDE LENGTHS, NUMBER OF NODES AND ELEMENTS IN THE SPATIAL DISCRETIZATION, LENGTH OF TIME STEP Δt , AND NUMBER OF TIME POINTS M IN THE TEMPORAL DISCRETIZATION

Δh (μm)	Nodes	Elements	Δt (ns)	M
96 ± 16	728213	4112879	26.6	387

memory requirements, the results could not be compared against the conventional approach where the whole forward operator would have been formulated. The forward operator K_{CNV} would have required 2919.6 GB of memory. Therefore, to provide a comparison, a time-reversal reconstruction was computed. It is presented in the supplementary material.

C. Results

Cross-sections of the MAP-estimate computed from the experimental data are shown in Fig. 7. As it can be seen, the knot and the two loops are clearly visible. It can, however, be seen that the elevational (z -directional) resolution of the reconstruction is worse compared to the lateral and axial resolution in the xy plane. The loop of the knot, which is located approximately in the xy plane, can be distinguished in several slices even though it should be visible in only a single slice. This reduction in resolution is due to the measurement setup and more specifically due to the features of the ultrasound transducer (cylindrical focus) and the measurement geometry. Furthermore, as the target is illuminated from the top, most of the light within the z -directional loop is absorbed into the top-most parts of the loop.

VI. DISCUSSION

In the transformation-based forward model, the forward operator is constructed for a single reference transducer and extended to a general measurement geometry using coordinate transformations and interpolations. These interpolations can lead to modeling errors when using coarse discretizations. In this work, it was found that when using discretizations relevant to the principal applications of PAT (in the range of $\lesssim 100 \mu\text{m}$), the modeling errors due to the interpolations were small both in the forward solutions and in the reconstructions. One should, however, note that the manifestation of the modeling errors in the reconstructed images is additionally dependent on the reconstructed target, i.e. the size and smoothness of the target with respect to the spatial discretization.

One of the major benefits of the transformation-based forward operator in the inverse problem of PAT is the significant reduction of memory requirements compared to the conventional forward operator. However, the inverse problem of PAT introduces additional memory requirements in the form of the prior distribution. The prior covariance matrix contains L^2 entries, where L is the number of the discretized initial pressure values and can thus potentially require significant amounts of

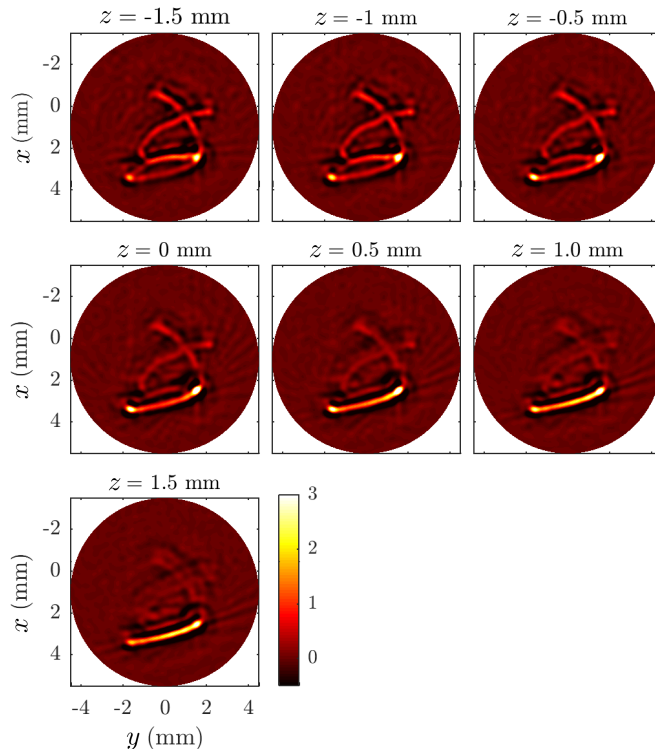


Fig. 7. Cross sectional images of the reconstruction using the data from the experimental phantom at vertical planes of $z = -1.5, -1.0, -0.5, 0, 0.5, 1.0$ and 1.5 mm.

memory. As an example, if the prior distribution is defined by a covariance matrix based on an exponential based distribution such as the Ornstein-Uhlenbeck process, the covariance matrix is, by definition, a full matrix. In this work, this problem was alleviated by using a piece-wise polynomial covariance matrix, which is sparse by nature. Furthermore, in this work, the prior information was implemented using a matrix-free approach where the implementation was performed row-wise as a series of dot products. This type of approach is, however, not optimal with respect to the computation time. Implementation of the prior distribution could be further improved by using a regular (cubic voxel-based) discretization and Fourier transform-based 3D convolutions [18].

The transformation based approach was implemented by storing the forward operator and the interpolation matrix to memory and using them in the iterations. This enables flexible implementation of the approach, as a single forward operator can be used alongside various interpolation matrices to compute reconstructions in different transducer geometries. On the other hand, the entries of the forward operator and the interpolation matrix could be computed in a matrix free fashion during the iterative process. This would reduce the memory requirements but could increase the computational time as the entries of these matrices would have to be computed repeatedly during each iteration.

In this work, the photoacoustic images were reconstructed iteratively using the general minimum residual method, that was found to converge to the correct solution. The optimality of this method was, however, not exhaustively studied. It was found that the convergence rate of the iteration was highly dependent on the complexity of the reconstructed target and the measurement geometry. As an example, reconstruction of the blood-vessel mimicking phantom simulation study took 83 iterations, whereas reconstruction of the experimental phantom took only 11 iterations.

In addition to PAT, the proposed method of formulating the forward model using the transformation based approach could also be used in applications such as thermoacoustic tomography.

VII. CONCLUSION

In this work, a transformation-based approach for modeling photoacoustic signals in PAT was proposed. The model was compared against the conventional forward model using simulations. Furthermore, the performance of the transformation-based forward model was studied in reconstructions using both simulated and experimental photoacoustic data. The results show that the transformation-based forward model is able to produce as accurate forward solutions as the conventional forward model in the limit of sufficient spatial and temporal discretization. Furthermore, the method is simple to implement and it can be straightforwardly implemented and utilized in various measurement geometries. The method reduces the computation cost of the PAT inverse problem significantly while maintaining the accuracy of the estimates when compared to the conventional approach.

REFERENCES

- [1] P. Beard, "Biomedical photoacoustic imaging," *Interface Focus*, vol. 1, no. 4, pp. 602–631, 2011.
- [2] L. V. Wang and J. Yao, "A practical guide to photoacoustic tomography in the life sciences," *Nat. Methods*, vol. 13, no. 8, pp. 627–638, 2016.
- [3] C. Li and L. V. Wang, "Photoacoustic tomography and sensing in biomedicine," *Phys. Med. Biol.*, vol. 54, no. 19, pp. R59–97, 2009.
- [4] J. Poudel, Y. Lou, and M. A. Anastasio, "A survey of computational frameworks for solving the acoustic inverse problem in three-dimensional photoacoustic computed tomography," *Phys. Med. Biol.*, vol. 64, p. 14TR01, 2019.
- [5] I. Steinberg, D. M. Huland, O. Vermesh, H. E. Frostig, W. S. Tummers, and S. S. Gambhir, "Photoacoustic clinical imaging," *Photoacoustics*, vol. 14, pp. 77–98, 2019.
- [6] A. B. E. Attia *et al.*, "A review of clinical photoacoustic imaging: Current and future trends," *Photoacoustics*, vol. 16, p. 100144, 2019.
- [7] L. A. Kunuansky, "Explicit inversion formulae for the spherical mean radon transform," *Inverse Probl.*, vol. 23, no. 1, pp. 373–383, 2007.
- [8] M. Xu, Y. Xu, and L. Wang, "Time-domain reconstruction algorithms and numerical simulations for thermoacoustic tomography in various geometries," *IEEE Trans. Med. Imaging*, vol. 50, no. 9, pp. 1086–1099, 2003.
- [9] M. Xu and L. V. Wang, "Universal back-projection algorithm for photoacoustic computed tomography," *Phys. Rev. E*, vol. 71, no. 016706, 2005.
- [10] L. A. Kunuansky, "A series solution and a fast algorithm for the inversion of the spherical mean radon transform," *Inverse Probl.*, vol. 23, no. 6, pp. 11–20, 2007.
- [11] Y. Xu and L. A. Wang, "Time reversal and its application to tomography with diffracting sources," *Phys. Rev. Lett.*, vol. 92, no. 3, p. 033902, 2004.
- [12] Y. Hristova, P. Kuchement, and L. Nguyen, "Reconstruction and time reversal in thermoacoustic tomography in acoustically homogeneous and inhomogeneous media," *Inverse Probl.*, vol. 24, no. 5, p. 055006, 2008.
- [13] S. R. Arridge, M. M. Betcke, B. T. Cox, F. Lucka, and B. E. Treeby, "On the adjoint operator in photoacoustic tomography," *Inverse Probl.*, vol. 32, no. 11, p. 115012, 2016.
- [14] X. L. Deán-Ben, A. Buehler, V. Ntziachristos, and D. Razansky, "Accurate model-based reconstruction algorithm for three-dimensional optoacoustic tomography," *IEEE Trans. Med. Imaging*, vol. 31, no. 10, pp. 1922–1928, 2012.
- [15] J. Zhang, M. A. Anastasio, J. L. Rivière, and L. Wang, "Effects of different imaging models on least-squares image reconstruction accuracy in photoacoustic tomography," *IEEE Trans. Med. Imaging*, vol. 28, no. 11, pp. 1781–1790, 2009.
- [16] C. Huang, K. Wang, L. Nie, L. V. Wang, and M. A. Anastasio, "Full-wave iterative image reconstruction in photoacoustic tomography with acoustically inhomogeneous media," *IEEE Trans. Med. Imaging*, vol. 32, no. 6, pp. 1097–1110, 2013.
- [17] J. Tick, A. Pulkkinen, and T. Tarvainen, "Image reconstruction with uncertainty quantification in photoacoustic tomography," *J. Acoust. Soc. Am.*, vol. 139, no. 4, pp. 1951–1961, 2016.
- [18] J. Tick *et al.*, "Three dimensional photoacoustic tomography in Bayesian framework," *J. Acoust. Soc. Am.*, vol. 144, no. 4, pp. 2061–2071, 2018.
- [19] T. Sahlström, A. Pulkkinen, J. Tick, J. Leskinen, and T. Tarvainen, "Modeling of errors due to uncertainties in ultrasound sensor locations in photoacoustic tomography," *IEEE Trans. Med. Imaging*, vol. 39, no. 6, pp. 2140–2150, 2020.
- [20] I. Olefir, S. Tzoumas, H. Yang, and V. Ntziachristos, "A Bayesian approach to eigenspectra optoacoustic tomography," *IEEE Trans. Med. Imaging*, vol. 37, no. 9, pp. 2070–2079, 2018.
- [21] M. A. A. Caballero, J. Gateau, and X. L. Deán-Ben, "Model-based optoacoustic image reconstruction of large three-dimensional tomographic datasets acquired with an array of directional detectors," *IEEE Trans. Med. Imaging*, vol. 33, no. 2, pp. 433–443, 2014.
- [22] C. Lutzweiler, X. L. Deán-Ben, and D. Razansky, "Expediting model-based optoacoustic reconstructions with tomographic symmetries," *Med. Phys.*, vol. 41, no. 1, p. 013302, 2014.
- [23] S. Bu *et al.*, "Model-based reconstruction integrated with fluence compensation for photoacoustic tomography," *IEEE Trans. Biom. Eng.*, vol. 59, no. 5, pp. 1354–1363, 2012.
- [24] K. Wang, C. Huang, Y.-J. Kao, C.-Y. Chou, A. A. Oraevsky, and M. A. Anastasio, "Accelerating image reconstruction in three-dimensional optoacoustic tomography on graphics processing units," *Med. Phys.*, vol. 40, no. 2, p. 023301, 2013.
- [25] L. Ding, X. L. Deán-Ben, and D. Razansky, "Efficient 3-d model-based reconstruction scheme for arbitrary optoacoustic acquisition geometries," *IEEE Trans. Med. Imaging*, vol. 36, no. 9, pp. 1858–1867, 2017.
- [26] S. Arridge *et al.*, "Accelerated high-resolution photoacoustic tomography via compressed sensing," *Phys. Med. Biol.*, vol. 61, no. 24, pp. 8908–8940, 2016.
- [27] M. Haltmeier, M. Sandbichler, T. Berer, J. Bauer-Marschallinger, P. Burgholzer, and L. Nguyen, "A sparsification and reconstruction strategy for compressed sensing photoacoustic tomography," *J. Acoust. Soc. Am.*, vol. 143, no. 6, pp. 3838–3848, 2018.
- [28] C. Lutzweiler, S. Tzoumas, A. Rosenthal, V. Ntziachristos, and D. Razansky, "High-throughput sparsity-based inversion scheme for optoacoustic tomography," *IEEE Trans. Med. Imaging*, vol. 35, no. 2, pp. 674–684, 2016.
- [29] J. Zalev and M. C. Kolios, "Fast three-dimensional opto-acoustic simulation for linear array with rectangular elements," *IEEE Trans. Ultrason. Ferroelec. Freq. Contr.*, 2019, doi: 10.1109/TUFFC.2020.3038622.
- [30] J. Tick, A. Pulkkinen, and T. Tarvainen, "Modelling of errors due to speed of sound variations in photoacoustic tomography using a Bayesian framework," *Biomed. Phys. Eng. Express*, vol. 6, no. 1, p. 015003, 2019.
- [31] V. Z. Gusev and A. A. Karabutov, *Laser optoacoustics*. College Park, MD, USA: Chapman & Hall, 1992.
- [32] A. Pulkkinen, B. T. Cox, S. R. Arridge, H. Goh, J. P. Kaipio, and T. Tarvainen, "Direct estimation of optical parameters from photoacoustic time series in quantitative photoacoustic tomography," *IEEE Trans. Med. Imaging*, vol. 35, no. 11, pp. 2497–2508, 2016.
- [33] D. G. Duffy, *Green's Functions With Applications*. Boca Raton, FL, USA: Chapman & Hall, 2001.
- [34] B. E. Treeby and B. T. Cox, "k-Wave: Matlab toolbox for the simulation and reconstruction of photoacoustic wave-fields," *J. Biomed. Opt.*, vol. 15, no. 2, p. 021314, 2010.
- [35] J. P. Kaipio and E. Somersalo, *Statistical and Computational Inverse Problems*. New York, NY, USA: Springer, 2005.
- [36] C. E. Rasmussen and C. K. I. Williams, *Gaussian Processes for Machine Learning*. Massachusetts, MA, USA: MIT Press, 2006.
- [37] P. Lai, X. Xu, and L. Wang, "Dependence of optical scattering from intralipid in gelatin-gel based tissue-mimicking phantoms on mixing temperature and time," *J. Biomed. Opt.*, vol. 19, no. 3, p. 35002, 2014.
- [38] P. D. Ninni, F. Martelli, and G. Zaccanti, "The use of india ink in tissue-simulating phantoms," *Opt. Express*, vol. 18, no. 26, pp. 854–865, 2010.
- [39] S. Grabtchak, T. Palmer, F. Foschum, A. Liemert, A. Kienle, and W. Whelan, "Experimental spectro-angular mapping of light distribution in turbid media," *J. Biomed. Opt.*, vol. 17, no. 6, p. 067007, 2012.
- [40] K. Mitsuhashi, K. Wang, and M. A. Anastasio, "Investigation of the far-field approximation for modeling a transducer's spatial impulse response in photoacoustic computed tomography," *Photoacoustics*, vol. 2, no. 1, pp. 21–32, 2014.



Teemu Sahlström received his B.Sc. degree in medical physics from the University of Eastern Finland in 2017 and his M.Sc. degree in computational physics from the University of Eastern Finland in 2019. He is currently an early stage researcher and working on his Ph.D. at the Department of Applied Physics, University of Eastern Finland. His research interests include photoacoustic tomography, numerical methods, computational physics and inverse problems.



Aki Pulkkinen is a senior scientist at the Department of Applied Physics in the University of Eastern Finland, from which he received his Ph.D. degree on the subject of transcranial focused ultrasound therapy. His research interests include modeling of optical and ultrasonic propagation, therapeutic applications of ultrasound, optoacoustic and acousto-optic imaging and tomography, and related inverse problems.



Jarkko Leskinen is a postdoctoral researcher in the University of Eastern Finland. He received his Ph.D. degree in medical physics from the University of Eastern Finland. Topic of his doctoral thesis was ultrasound therapy on bone and cartilage. His research interests include ultrasonics, photoacoustic imaging and diffuse optical imaging.



Tanja Tarvainen received the M.Sc. and the Ph.D. degrees in physics from the University of Kuopio, Finland, in 2000 and 2006, respectively. After completion of her degrees, she worked as a Postdoctoral Research Associate at the University College London, U.K. and a postdoctoral researcher at the University of Kuopio. She was an Academy Research Fellow and an Associate Professor in the University of Eastern Finland, in 2011-2015 and 2017-2020, respectively. She currently is a Professor of computational imaging and modeling at the Department of Applied Physics in the University of Eastern Finland. Her research interests include computational and Bayesian inverse problems, and uncertainty quantification with applications in optical imaging.